White Rose Research Online

eprints@whiterose.ac.uk
https://eprints.whiterose.ac.uk
Universities of Leeds, Sheffield and York

Deposited via The University of Sheffield.

White Rose Research Online URL for this paper:
https://eprints.whiterose.ac.uk/id/eprint/154785/

Version: Published Version

Article:
Zheng, K., Balasubramanian, P., Paterson, T.E. et al. (2019) Ag modified mesoporous bioactive glass nanoparticles for enhanced antibacterial activity in 3D infected skin model. Materials Science and Engineering: C, 103. 109764. ISSN: 0928-4931

https://doi.org/10.1016/j.msec.2019.109764

Reuse
This article is distributed under the terms of the Creative Commons Attribution (CC BY) licence. This licence allows you to distribute, remix, tweak, and build upon the work, even commercially, as long as you credit the authors for the original work. More information and the full terms of the licence here: https://creativecommons.org/licenses/

Takedown
If you consider content in White Rose Research Online to be in breach of UK law, please notify us by emailing eprints@whiterose.ac.uk including the URL of the record and the reason for the withdrawal request.

UNIVERSITY OF LEEDS
University of Sheffield
UNIVERSITY of York

Materials Science & Engineering C 103 (2019) 109764

Contents lists available at ScienceDirect

Materials Science & Engineering C

journal homepage: www.elsevier.com/locate/msec

Ag modified mesoporous bioactive glass nanoparticles for enhanced antibacterial activity in 3D infected skin model

Kai Zheng[a], Preethi Balasubramanian[a], Thomas E. Paterson[b], Rene Stein[a], Sheila MacNeil[c], Sonia Fiorilli[d], Chiara Vitale-Brovarone[d], Joanna Shepherd[b], Aldo R. Boccaccini[a,*]

[a] Institute of Biomaterials, University of Erlangen-Nuremberg, Erlangen, Germany
[b] School of Clinical Dentistry, The University of Sheffield, Sheffield, United Kingdom
[c] Department of Materials Science & Engineering, The Kroto Research Institute, University of Sheffield, Sheffield, United Kingdom
[d] Department of Applied Science and Technology, Politecnico di Torino, Turin, Italy

ARTICLE INFO

Keywords:
Silver
Bioactive glasses
Nanoparticles
Antibacterial activity
3D skin model

ABSTRACT

Bioactive glasses (BG) are versatile materials for various biomedical applications, including bone regeneration and wound healing, due to their bone bonding, antibacterial, osteogenic, and angiogenic properties. In this study, we aimed to enhance the antibacterial activity of SiO_2-CaO mesoporous bioactive glass nanoparticles (MBGN) by incorporating silver (Ag) through a surface modification approach. The modified Ag-containing nanoparticles (Ag-MBGN) maintained spherical shape, mesoporous structure, high dispersity, and apatite-forming ability after the surface functionalization. The antibacterial activity of Ag-MBGN was assessed firstly using a planktonic bacteria model. Moreover, a 3D tissue-engineered infected skin model was used for the first time to evaluate the antibacterial activity of Ag-MBGN at the usage dose of 1 mg/mL. In the planktonic bacteria model, Ag-MBGN exhibited a significant antibacterial effect against both *Pseudomonas aeruginosa* and *Staphylococcus aureus* in comparison to non-engineered (Ag-free) MBGN and the blank control. Moreover, Ag-MBGN did not show cytotoxicity towards fibroblasts at the usage dose. However, in the 3D infected skin model, Ag-MBGN only demonstrated antibacterial activity against *S. aureus* whereas their antibacterial action against *P. aeruginosa* was inhibited. In conclusion, surface modification by Ag incorporation is a feasible approach to enhance the antibacterial activity of MBGN without significantly impacting their morphology, polydispersity, and apatite-forming ability. The prepared Ag-MBGN are attractive building blocks for the development of 3D antibacterial scaffolds for tissue engineering.

1. Introduction

Bioactive glasses (BGs) are promising materials for a variety of tissue regeneration strategies, owing to their biocompatibility, osteogenic and angiogenic activities [1,2]. Nanoscale BGs, including nanoparticles and nanofibers, are particularly attractive materials in biomedical applications, due to their morphological advantages (*e.g.*, small dimension, uniform size, controllable shape) [3,4]. For example, BG nanoparticles can be applied as advanced bioactive fillers in coatings [5], scaffolds [6], and hydrogels [7], to enhance the functionalities of matrices (*e.g.*, mechanical properties, biomineralization ability, osteogenesis). Among various nanoscale BGs, mesoporous bioactive glass nanoparticles (MBGN) attract increasing attention as bioactive fillers or drug carriers in tissue regeneration or nanomedicine applications because of their tunable size/pore structure, large specific surface area (SSA), and large surface-to-volume ratio [3]. Besides morphology, the chemical composition of BGs can also be tailored for specific applications [8,9]. For example, silver (Ag) can be incorporated into BGs to enhance their antibacterial activity [10,11].

Bacteria-induced infections remain major clinical challenges for effective tissue repair/regeneration [12]. For example, bone implants are commonly associated with a risk of bacterial adherence and colonization, which may cause prolonged healing or implantation failure [13]. Many efforts have been dedicated to reduce or eliminate the risk of bacteria-induced infections. Antibiotics are currently the primary solution to kill bacteria. However, bacteria can continuously evolve and exhibit resistance to antibiotics, which can compromise the antibacterial effects of such drugs [14]. Alternatively, the clinical use of materials with intrinsic antibacterial activities may avoid the risk of infections without the problem of bacterial resistance [15–17].

* Corresponding author.
E-mail address: aldo.boccaccini@fau.de (A.R. Boccaccini).

https://doi.org/10.1016/j.msec.2019.109764
Received 3 January 2019; Received in revised form 15 May 2019; Accepted 16 May 2019
Available online 17 May 2019
0928-4931/ © 2019 The Authors. Published by Elsevier B.V. This is an open access article under the CC BY license (http://creativecommons.org/licenses/BY/4.0/).

Conventional BG compositions, *e.g.*, 45S5 and S53P4 BGs, have shown antibacterial effects by increasing local pH during glass dissolution [18,19]. However, such effects may also cause toxicity towards mammalian cells [20]. Novel compositions that can selectively exert significant toxic effects only on bacteria are thus highly demanded in tissue regeneration. Metal ions have been used as antibacterial agents for a long time [17], among which Ag has demonstrated an effectively broad-spectrum bactericidal activity [21]. Incorporation of Ag has been proven to be a feasible approach to enhance the antibacterial activity of BGs [22,23].

Two strategies, namely the one-step and post-modification methods, have been used to synthesize Ag-containing (mesoporous) bioactive glass nanoparticles (BGN). In the former strategy, Ag precursors (usually soluble silver salts) are added during the formation and growth of BGN [24] while Ag is incorporated after the formation of BGN in the latter method [25]. The post-modification approach, which has the advantage of retaining the shape, size and dispersity of the synthesized nanoparticles, has been applied to incorporate various metal ions (*e.g.*, Ca, Ag) into BGN [25,26]. However, the synthesis of Ag-containing MBGN has not been extensively explored [10,11,27]. Ag-containing MBGN have been synthesized using a one-step strategy, in which all precursors and templates react together. However, the resultant nanoparticles may suffer from aggregation and inhomogeneity in size or shape [11,27], which can compromise applications where dispersity and homogeneity in particle size and shape are required.

In this study, we applied a post-modification approach to engineer MBGN surfaces by incorporating Ag to enhance the antibacterial activity of MBGN. After the surface modification, MBGN maintained the morphology, mesopore structure, dispersity, and apatite-forming ability, while Ag could be successfully incorporated into MBGN. The antibacterial activity of Ag-containing BGs has been extensively assessed using different bacterial strains in planktonic bacteria models where a single type of bacteria is usually considered [22,28]. However, such models do not accurately reflect the actual microenvironment of infected tissues in wounds *in vivo*. On the other hand, a 3D infected skin model can mimic intricate interactions occurring *in vivo*, where bacteria invade and interact with other cell types [29]. We thus evaluated the antibacterial activity of the novel Ag-containing MBGN using a 3D tissue-engineered infected skin model for the first time. The results obtained in such a model are expected to reflect more accurately the actual antibacterial behavior of Ag-MBGN in infected tissues.

2. Materials and methods

2.1. Synthesis of MBGN

MBGN (a binary SiO_2-CaO composition) were synthesized using a microemulsion-assisted sol-gel method as reported in the literature [30]. Briefly, 0.7 g of hexadecyl trimethyl ammonium bromide (CTAB; ≥97%, Merck) was dissolved in 33 mL of deionized water while stirring. After the solution became clear, 10 mL of ethyl acetate (≥99.8%, Merck) was added to form microemulsion droplets, followed by further stirring for 30 min. Then, 0.47 mL of aqueous ammonia (28%, VWR Chemicals) was added and stirred for another 15 min. In intervals of 30 min, 3.6 mL of tetraethyl orthosilicate (TEOS, 99%, Sigma-Aldrich) and 2.56 g of calcium nitrate tetrahydrate (99.5%, VWR Chemicals) were added slowly to the mixture and stirred for 4 h. The mixture gradually became whitish due to the formation of colloidal particles. The particles were collected by centrifugation at 7,197 × *g* (Centrifuge 5430R, Eppendorf, Germany) for 15 min and washed twice with deionized water and once with ethanol (96%, VWR Chemicals). The collected particles were then dried at 60 °C overnight before calcination at 600 °C for 6 h with a heating rate of 2 °C/min.

2.2. Surface modification of MBGN

The prepared MBGN were modified by using an impregnation approach similar to the method reported previously [25]. Briefly, as-synthesized MBGN were soaked in 0.05 M silver nitrate (99%, VWR Chemicals) isopropanol solution (70% in water, VMR Chemicals) for 20 min at a concentration of 1 mg/mL. The soaked particles were then collected by centrifugation (7,197 × *g* for 15 min) and washed twice with deionized water and once with ethanol to remove the loosely bonded silver nitrate. After washing, the particles were dried at 60 °C for 3 h before calcination at 550 °C for 1 h (heating rate of 2 °C/min) to stabilize Ag. The obtained particles were then labeled as Ag-MBGN. Many processing parameters, including soaking temperature, solvent type, and concentration of the solution, can affect the amount of incorporated Ag [25,31,32]. However, in this study, we mainly focused on the antibacterial activity of the nanoparticles, and a fixed impregnation condition was thus selected based on preliminary results [25].

2.3. Particle characterization

The morphology and microstructure of nanoparticles were characterized by using scanning electron microscopy (SEM) (Auriga, Zeiss, Germany) under an accelerating voltage of 2 kV. The particle size was determined according to SEM images using ImageJ (NIH, USA) and the number of counted particles was > 300. The chemical compositions of MBGN and Ag-MBGN were estimated using energy dispersive X-ray (EDX) spectroscopy (X-Max^N, Oxford Instruments). The surface charge, dynamic light scattering (DLS) particle size, and polydispersity index (PDI) of the nanoparticles were measured using a Zetasizer Nano ZS (Malvern Instruments, UK) instrument with a 4 mW HeNe laser (633 nm) and a light scattering detector positioned at 90°. The measurements were performed in Dulbecco phosphate buffered saline (PBS, pH ~7.3, Gibco) at a concentration of 1 mg/mL. The samples were also characterized by Fourier transform infrared spectroscopy (FTIR, Nicolet 6700, Thermo Fisher Scientific) to assess their chemical structure. For FTIR measurements, particles mixed with KBr (WR Chemicals) were pressed to pellets at a weight ratio of 1:100. X-ray diffraction (XRD) analysis was performed using a D8 ADVANCE X-ray diffractometer (Bruker, USA) in a 2θ range of 20–80° with Cu *Kα* radiation. The particles were dispersed in ethanol before being deposited on low-background silicon wafers (Bruker AXS). A step size of 0.02° with a dwell time of 1 s per step was used. The Brunauer-Emmett-Teller (BET) SSA and pore size distribution of the nanoparticles were determined using the nitrogen sorption method at 77 K, conducted on a Micromeritics porosimeter (Tristar 3000, Micro-metrics Instrument Corp., USA).

2.4. In vitro apatite formation

The apatite-forming ability of Ag-MBGN was evaluated by soaking the nanoparticles in simulated body fluid (SBF) for up to 7 days at a concentration of 1 mg/mL and kept in an incubator (KS 4000i control, IKA, Germany) at 37 °C shaking at 90 rpm. At predetermined time points, the particles were collected and rinsed with acetone before drying at 60 °C overnight. The SBF was prepared as reported by Kokubo et al. [33]. The formation of apatite on the particles was characterized by SEM, FTIR, and XRD. The characterization procedure was the same as described above.

2.5. Release of Ag^+ ions

The ion release ability of Ag-MBGN was evaluated in physiological fluid PBS. Briefly, 10 mg of Ag-MBGN were dispersed in PBS at the concentration of 1 mg/mL and kept in an incubator at 37 °C shaking at 90 rpm. After 24 h, 5 mL of the supernatant was collected by centrifugation at 7830 rpm for 20 min and filtration using 0.2 μm filters (VMR, Germany). The concentration of Ag^+ ions in the supernatant was

measured by inductively coupled plasma-optical emission spectrometry (ICP-OES) using Agilent ICP-OES 720 instrument (Agilent, USA).

2.6. In vitro cytotoxicity

Fibroblast 3T3 cells (Sigma-Aldrich, UK) were cultured in high glucose Dulbecco's modified Eagle's medium (DMEM) (Sigma-Aldrich, UK) supplemented with 100 U/mL of penicillin (Sigma-Aldrich, UK) and 1 mg/mL of streptomycin (Sigma-Aldrich, UK) at 37 °C in a humidified incubator equilibrated with 5% CO_2. Cells were seeded at a density of 1×10^4 into a 96-well plate and incubated at 37 °C for 24 h. The glass particles were sterilized by heating at 160 °C and stored under sterile conditions before being added to the fresh medium at the specified concentrations (1 mg/mL and 4 mg/mL). The cell culture medium was removed and 200 µL of sample medium was added in triplicate to the cells, and this mixture was incubated for 24 h. The PrestoBlue metabolic assay was used to quantify the metabolic activity of the cells exposed to the samples. PrestoBlue (Sigma-Aldrich, UK) was mixed with DMEM to form 10% (v/v) stock solution and this working solution then replaced the overnight solution containing the samples. The PrestoBlue solution was incubated for 60 min before conducting fluorescence measurements. Three technical repeats (n) were used within each experiment that was repeated in triplicate (N).

2.7. In vitro antibacterial activity

2.7.1. Bacterial strains

Clinical isolates of *Pseudomonas aeruginosa* (SOM1) and *Staphylococcus aureus* (S-235) were cultured in 20 mL Brain Heart Infusion (BHI; Oxoid, Basingstoke, UK) broth at 37 °C for 24 h from stock plates before use.

2.7.2. Planktonic bacteria model

Overnight cultures of *S. aureus* and *P. aeruginosa* bacteria were adjusted to an optical density of 1.0 at 600 nm and then diluted (1:10) in fresh BHI broth before experimental use. The sterilized samples (MBGN and Ag-MBGN) were weighed and added to fresh BHI broth to a final concentration of 1 mg/mL. 100 µL of diluted overnight bacteria suspension was combined with 100 µL of sample suspension in a well in a 96-well plate. The control was broth without samples added. The well plate was left to incubate overnight at 37 °C. The remaining viable bacteria following incubation with particles were counted using the Miles and Misra method [34]. Three technical repeats (n) were used within each experiment, which was repeated in triplicate (N).

2.7.3. 3D tissue engineered infected skin model

A 3D tissue engineered infected skin model was established as reported previously [29,35]. Fig. 1 shows the schematic of the antibacterial test in the 3D tissue engineered infected skin model. Briefly, the tissue-engineered skin was first grown and then infected with the microorganism to test the antibacterial effectiveness of the samples. Glycerol preserved human cadaver skin (Euro Skin, Netherlands) was rinsed in PBS for 7 days to remove the glycerol, with a change in PBS each day. The skin was then incubated in 0.1 M NaCl at 37 °C for 24 h or until the epidermis could be easily separated from the dermis using blunt forceps. The epidermis was discarded and the de-epithelialized dermis (DED) then stored in Greens media: DMEM high glucose (4500 mg/L glucose) and Ham's F12 medium in a 3:1 ratio, 10% v/v FCS (UK), 10 ng/mL human recombinant epidermal growth factor, 0.4 mg/mL hydrocortisone, 18 mM adenine, 5 mg/mL insulin, 5 mg/mL apo-transferrin, 20 mM 3,3,5-triiodothyronine, 2 mM glutamine, 0.625 mg/mL amphotericin B, 100 U/mL penicillin, and 1000 mg/mL streptomycin. An 11 mm diameter cork borer and a scalpel were used to cut 11 mm disks from the DED to use for the model. These disks were placed in the bottom of a Transwell plate well (Millicell Hanging Cell Culture Insert, PET 0.4 µm, 12-well). Primary human dermal fibroblasts were isolated from split-thickness skin biopsies (as per previously published protocols [29]) received from abdominoplasties and breast reductions performed at the Northern General Hospital, Sheffield. Research Ethics approval was obtained from the Sheffield Research Ethics Committee. 1×10^5 fibroblasts and 3×10^5 HaCat keratinocytes (Thermo Fisher Scientific, UK) were added to the surface of the DED in 500 µL of Greens media. The media was replaced after 24 h and then removed after a further 24 h. 1 mL of Greens medium was added around the insert to establish an air-liquid interface. This medium was replaced every 2 days for a total of 21 days, allowing the model to mature. A cautery pen (Aaron medical) was applied for 8 s to the surface of the 3D model to burn a portion of the surface. 1×10^6 bacteria cells in 20 µL of BHI broth from an overnight culture were added to the models and incubated for 24 h to allow the infection to establish. Ag-MBGN were prepared to 1 mg/mL in 200 µL of broth and added to the model. The plates were then incubated for 24 h. Broth only was used for the control group. The 3D model was removed from the inserts, weighed, and diced with a scalpel for 60 s. Samples were transferred to an Eppendorf with 1 mL of PBS and vortexed for 30 s. The Miles and Misra method was then used to count the colony forming units. Three technical repeats were used for a single experiment.

3. Results and discussion

3.1. Synthesis and characterization

Fig. 2 shows SEM images of MBGN and Ag-MBGN. Both nanoparticles, whose sizes appeared to be in the range of 100 to 250 nm,

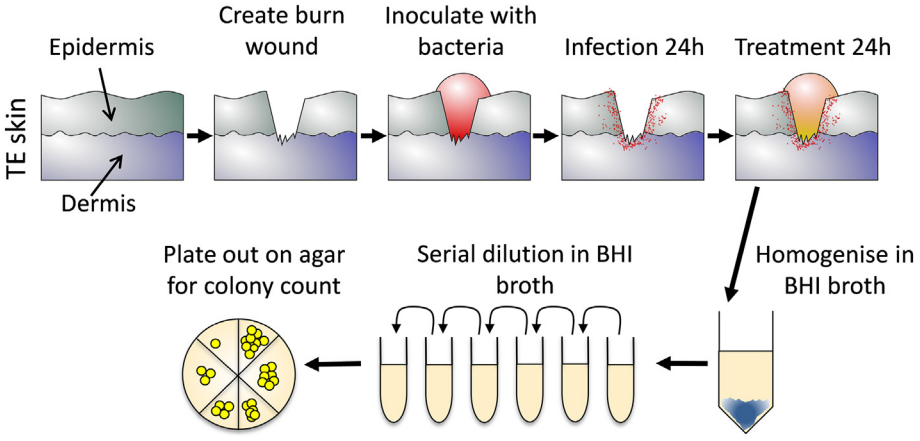

Fig. 1. Schematic of the antibacterial test in the 3D tissue engineered (TE) infected skin model.

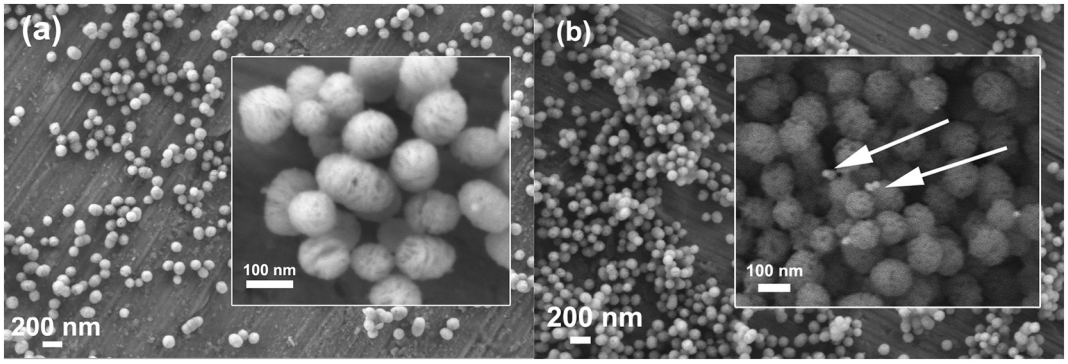

Fig. 2. SEM images of MBGN (a) before and (b) after surface modification (Ag-MBGN) at different magnifications. Arrows indicate the presence of Ag NPs.

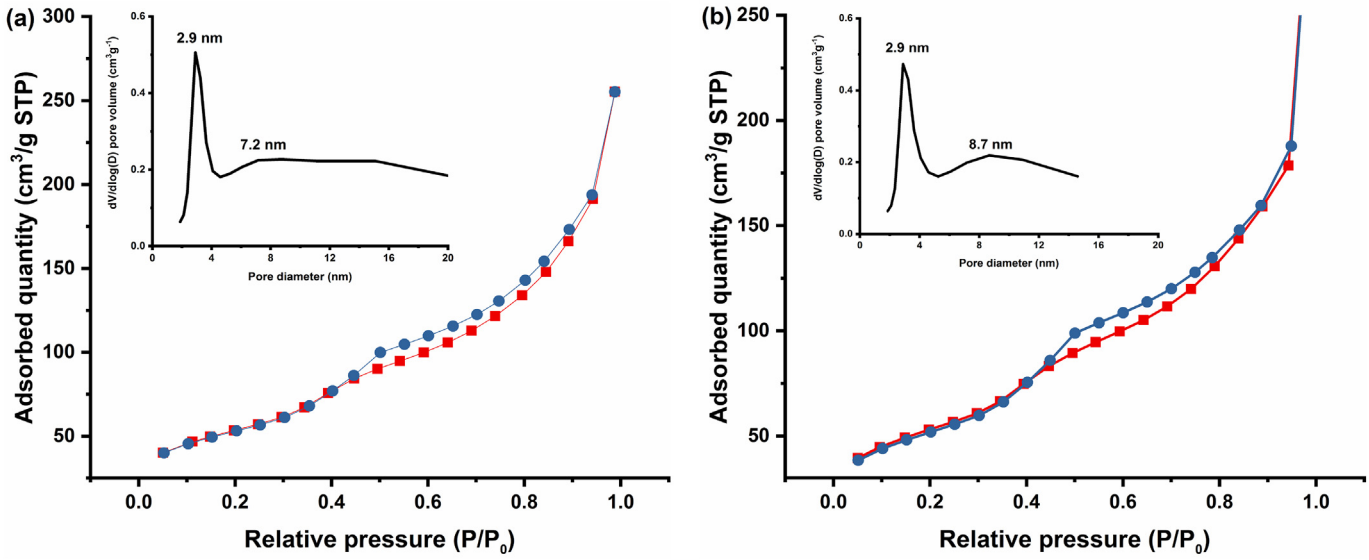

Fig. 3. N_2 adsorption-desorption isotherms and inserted pore size distribution curves for (a) MBGN and (b) Ag-MBGN.

exhibited sphere-like or ellipsoid-like shape with mesopores on their surfaces (Fig. 2). As expected, the size and shape of the nanoparticles were not entirely uniform, which is commonly found in nanoparticles obtained through the microemulsion method, due to the fusion and deformation of microemulsion droplets during the synthesis [30]. However, smaller nanoparticles that could be ascribed to metallic Ag nanoparticles (NPs) were observed in the SEM image of Ag-MBGN (Fig. 2b), but they were absent in the SEM image of MBGN. The N_2 adsorption-desorption isotherm of the obtained MBGN and Ag-MBGN (Fig. 3) exhibited a type IV isotherm as defined by IUPAC [36], which is a typical isotherm for nanoporous materials. However, MBGN showed a heterogeneous pore size distribution, which displayed a narrow pore size distribution centered at 2.9 nm but also a wide distribution starting from 4 nm (Fig. 3a). Such relatively large pores could also be observed in the SEM images of MBGN (Fig. 2a). After the surface treatment, Ag-MBGN maintained the narrow pore size distribution at ~2.9 nm (Fig. 3b) and the wide distribution centered at ~8.7 nm. The pores of Ag-MBGN appeared to be slightly enlarged, probably because of the solvent causing the dissolution of pore walls during the surface modification process [37]. As in the case of pore size, the pore volume of nanoparticles (Table 1) was also slightly enlarged (from 0.39 to 0.49 cm^3/g) after the surface modification. However, the SSA of the nanoparticles was reduced from 320 m^2/g to 262 m^2/g (Table 1), probably due to the coverage of some mesopores by Ag NPs [38]. Overall, after the surface modification, the nanoparticles maintained their shape and mesoporous structure and still exhibited large SSA and pore volume, which are attractive for a variety of biomedical applications, such as drug delivery.

Table 1
Physicochemical characterization results for MBGN and Ag-MBGN.

Sample code	Zeta potential (mV)	DLS size (nm)	PDI	SSA (m^2/g)	Pore volume (cm^3/g)
MBGN	−26.3 ± 3.1	227 ± 13	0.121	320	0.39
Ag-MBGN	−22.9 ± 1.6	216 ± 6	0.257	262	0.49

The XRD pattern of Ag-MBGN (Fig. 4a) confirmed the presence of metallic Ag NPs, as four diffraction peaks located at 2θ = 38°, 44°, 65°, 78°, which could be attributed to (111), (200), (220) and (311) crystallographic planes of metallic Ag (JCPD 65-2871), were observed [27]. Before Ag incorporation, the nanoparticles, as expected, were fully amorphous, as only two broad bands located in the range between 2θ = 20–25° and 28–33°, ascribed to the silicon wafers used as the substrate, could be observed. FTIR spectra (Fig. 4b) of the particles showed characteristic bands of silicate glasses. Two bands located at ~460 cm^{-1} and 796 cm^{-1} could be attributed to Si–O–Si rocking vibration and Si–O–Si bending vibration, respectively, and the broadband in the 1000–1200 cm^{-1} range was ascribed to the Si-O-Si stretching vibration. The presence of these components indicated that [SiO_4] tetrahedrons had formed to build the glass network of the particles [39]. A slight shoulder located at ~946 cm^{-1} could also be noticed, which indicated the presence of Si–O–NBO (non-bridging oxygen) stretching [39]. The non-bridging oxygen structure is caused by network modifiers in silicate glasses, indicating that in the present particles

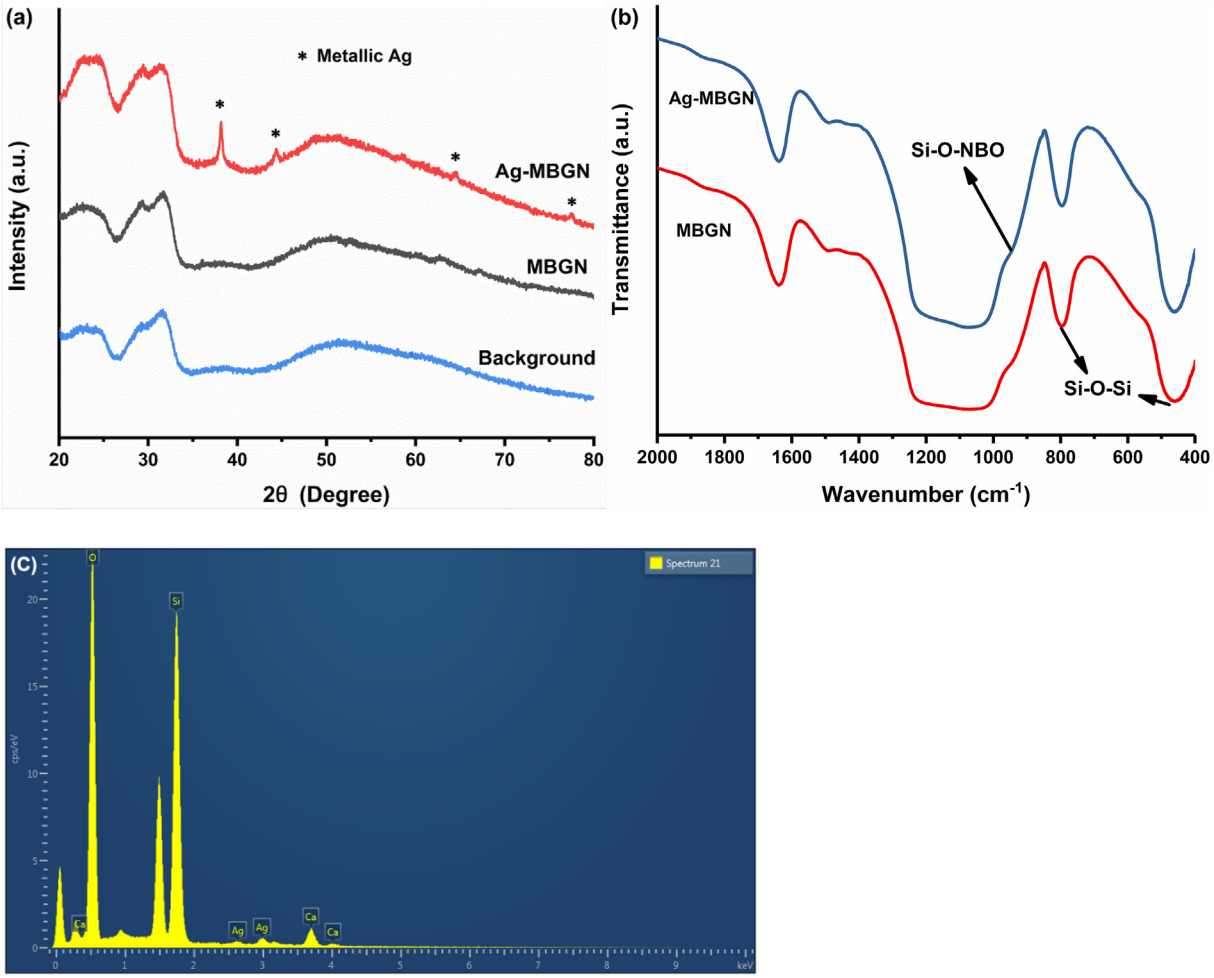

Fig. 4. (a) XRD patterns and (b) FTIR spectra of MBGN and Ag-MBGN; (c) EDS spectrum of Ag-MBGN showing the presence of Ag after the surface modification treatment.

calcium has entered the silicate network. Additionally, this shoulder did not change notably after the surface treatment, suggesting that Ag did not enter the silicate structure. A small band at ~1490 cm^{-1} could be observed in both spectra of MBGN and Ag-MBGN, which could be assigned to CO_3^{2-} antisymmetric stretching mode [39]. The appearance of this band could be attributed to the formation of carbonates on BG surfaces in the presence of atmospheric CO_2 due to the high reactivity of sol-gel derived BGs [40]. Table 1 shows the zeta potential, DLS particle size, and PDI of MBGN and Ag-MBGN in PBS (pH ~7.3, at 25 °C). Both types of particles exhibited negative surface charge, and their hydrodynamic sizes were slightly larger than the sizes observed in SEM images. The surface modification with Ag did not significantly influence the particle size whereas the PDI increased from 0.121 to 0.257 after the modification. The higher PDI of Ag-MBGN suggested a reduced dispersity of nanoparticles after surface modification, which was probably caused by the formed Ag NPs acting as bridging agents among the particles [41].

Silver nitrates can be easily reduced to metallic Ag NPs by chemical reducing agents [31], X-ray [42] or high-temperature treatment [38]. Reduction of silver nitrate has been used to functionalize BG surfaces [31,42]. In our previous study [25], we incorporated a relatively small amount of Ag into BGN, by which the formation of Ag NPs was avoided after heat treatment. The modified BGN maintained the amorphous feature, but their antibacterial activity was compromised due to the low content of Ag. In this study, the composition of MBGN was determined to be ~86SiO_2-14CaO (mol%) by the EDS analysis. After the surface modification, a band related to Ag could be observed in the EDS spectrum of Ag-MBGN (Fig. 4c), and the composition, as estimated by EDS, was ~87SiO_2-10.4CaO-2.6Ag_2O (mol%). Such an amount of Ag has been reported to exert effectively antibacterial activity while retaining the bioactivity of BGs [22,24]. Furthermore, in the literature, it has been reported that Ag concentration higher than 1 mol% in BGN could lead to the formation of metallic Ag besides the incorporation of Ag^+ upon heat treatment [43,44]. In accordance with these findings, Ag NPs were observed in the synthesized Ag-MBGN after heat treatment due to the relatively high concentration of Ag incorporated, while Ag^+ ions were also available in Ag-MBGN. For what concerns antibacterial activity, the co-existence of Ag^+ and Ag NPs may lead to enhanced and sustained antibacterial effects. Indeed, Ag^+ ions have been reported to be more effective in antibacterial action [45] while Ag NPs may endow MBGN with a long-term antibacterial activity as metallic Ag NPs dissolve slowly under physiological conditions [21]. Additionally, Ag NPs may also impact antibacterial effects by generating continuous reactive oxygen species (ROS) against bacterial cells [46].

3.2. *In vitro* apatite-forming ability

We further evaluated the apatite-forming ability of the particles after Ag incorporation, as this property (an indicator of bioactivity, related to the *in vivo* bone bonding ability) is one of the most characteristic features of BGs [47]. The formation of calcium phosphate species in Ag-MBGN after soaking in SBF was confirmed by FTIR analysis (Fig. 5a). Compared to the spectrum of non-soaked nanoparticles (Fig. 4a), two new bands located at ~560 cm^{-1} and ~600 cm^{-1} were

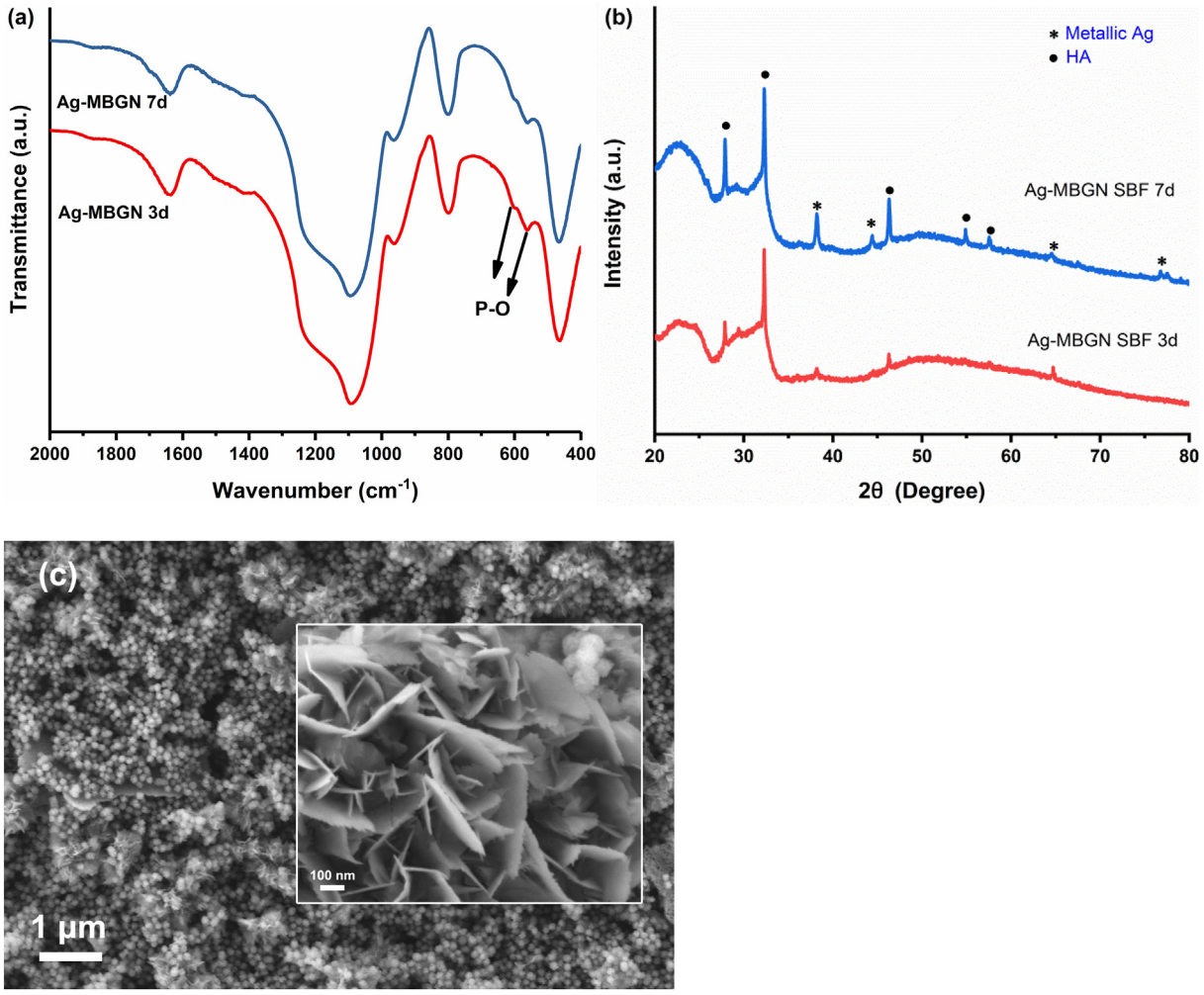

Fig. 5. Results of *in vitro* apatite-forming evaluation of Ag-MBGN in SBF: (a) FTIR spectra and (b) XRD patterns of Ag-MBGN after soaking in SBF for 3 days and 7 days; (c) SEM images of Ag-MBGN after soaking in SBF for 14 days at different magnifications.

present in the FTIR spectra of Ag-MBGN after soaking in SBF for 3 days, which were correlated to the P–O bending vibrations in crystalline PO_3^{-4} [48]. The occurrence of such bands indicated the formation of crystalline calcium phosphate (apatite phase) on Ag-MBGN upon immersion in SBF. Furthermore, the single band at ~1490 cm^{-1} split into double bands at ~1420 cm^{-1} and ~1500 cm^{-1} during the soaking in SBF, which can be attributed to the formation of carbonates [40]. The phenomenon indicated that the formed calcium phosphate phase could be carbonate hydroxyapatite (HCA) rather than stoichiometric hydroxyapatite (HA). Also, the shoulder located at ~946 cm^{-1}, indicating the non-bridging oxygen in glasses, became a slight band at ~960 cm^{-1} already after 3 days in SBF. This phenomenon could be induced by the exchange of network modifying ions of the glass with the ions in SBF and some dissolution of the particles [49]. With the further dissolution of nanoparticles, more Si-O-Si bonds were broken, causing non-bridging oxygen groups detected by FTIR. XRD patterns (Fig. 5b) confirmed the formation of a crystalline structure on Ag-MBGN after soaking in SBF. Compared to the XRD pattern of Ag-MBGN before soaking in SBF, new diffraction peaks, located at 2θ = 27.9°,29.3°, 32°, 46.3°, 54.8°, and 57.5°, related to HA crystals (JCPD 84-1998) [27], were observed after soaking in SBF for 3 days. The intensity of these peaks in the XRD pattern became greater after 7 days in SBF, indicating the enhanced crystallinity of HA. Notably, diffraction peaks located at 2θ = 38°, 44°, 65° and 78° related to metallic Ag could still be observed after 7 days of soaking in SBF, indicating the stability of Ag NPs in physiological fluids. Fig. 5c shows representative SEM images of Ag-MBGN after soaking in SBF for 14 days. Needle-like crystals, displaying the characteristic morphology of HA crystals forming on BGs after soaking in SBF [41], could be clearly observed. It has been reported that the presence of Ag^+ in the structure of BGs could improve apatite-forming ability, as Ag^+ ions could act as nucleation sites for HA [50,51]. The presence of metallic Ag, even at a high dose (8 mol%), could also improve or at least preserve the apatite-forming ability of BGs [44]. In this study, the nanoparticles after surface modification exhibited apatite-forming ability and HA could form within 3 days after soaking in SBF, which was consistent with results published previously by other authors [50,51].

3.3. *In vitro* cytotoxicity

Before evaluating the antibacterial activity of Ag-MBGN, we first assessed the cytotoxicity of these nanoparticles, considering that their potential applications (*e.g.*, in wound healing) would involve contact with mammalian cells. Fig. 6 shows the metabolism of fibroblasts in culture with MBGN and Ag-MBGN at two different concentrations. At the higher concentration of 4 mg/mL, the presence of MBGN did not reduce the metabolic activity of cells compared to the control (culture of cells only). However, Ag-MBGN greatly reduced the metabolic activity of cells, indicating cytotoxicity of Ag-MBGN against fibroblasts at the tested concentration, which was in analogy with results reported in the literature showing that Ag-containing BGs exhibited cytotoxicity against both mammalian cells and bacteria if used at a relatively high concentration [52]. At the lower concentration of 1 mg/mL, neither

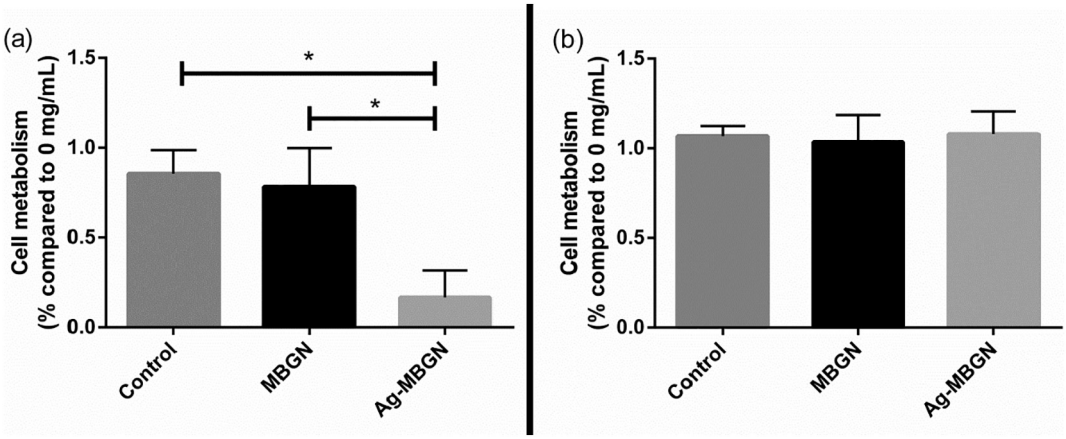

Fig. 6. Toxicity assay exposing the material to 3 t3 fibroblasts for 24 h. Metabolism was measured using Prestoblue and compared to a cell only control. Two different concentrations of material were used (a) 4 mg/mL and (b) 1 mg/mL. Three technical repeats (n = 3) were used within each experiment that was repeated in triplicate (N = 3). Data is presented as mean ± standard deviation (SD), and ANOVA was used for statistical analysis with * indicating $p < 0.05$.

MBGN nor Ag-MBGN reduced the metabolism of cells compared to the control, indicating non-cytotoxicity of the nanoparticles against fibroblasts at this concentration. The content of Ag in Ag-MBGN was calculated to be approximately 2.6 mol% by using EDS results. Such Ag content has been reported to have antibacterial effects while remaining non-cytotoxic towards mammalian cells [10,22,24]. However, a high dose of Ag-MBGN with such an Ag content (*e.g.*, 4 mg/mL) could still induce cytotoxicity, as indicated in this study. Nevertheless, the synthesized Ag-MBGN did not cause cytotoxicity towards fibroblasts at the concentration of 1 mg/mL, and this concentration was taken forward for antibacterial tests.

3.4. In vitro antibacterial activity

We first evaluated the antibacterial effects of Ag-MBGN against Gram-positive *S. aureus* and Gram-negative *P. aeruginosa* bacteria in a planktonic bacteria model. The presence of MBGN did not reduce colony forming units (CFU) of either bacterium compared to the control whereas Ag-MBGN had a high level of antibacterial activity as indicated by the significant Log reduction in CFU (Fig. 7). Ag-MBGN were effective against both *S. aureus* and *P. aeruginosa*, with no significant difference between the two species. The antibacterial activity of BG is heavily dependent on their chemical composition. It was expected that

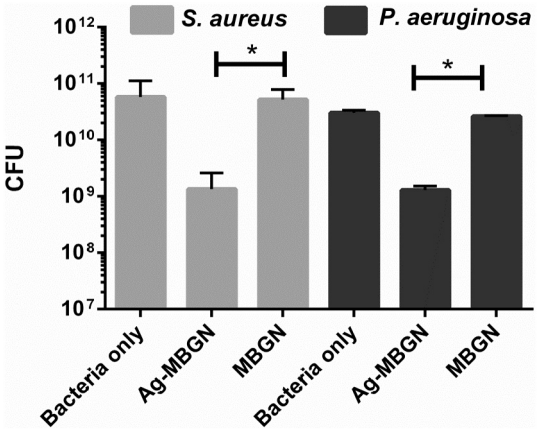

Fig. 7. Viable numbers of bacteria in colony forming units (CFU) in both *S. aureus* and *P. aeruginosa* bacteria after exposure to suspensions (1 mg/mL) of MBGN and Ag-MBGN for 24 h when compared to bacteria alone as control. Three technical repeats (n = 3) were used within each experiment that was repeated in triplicate (N = 3). Data presented as mean ± standard deviation (SD), and ANOVA was used for statistical analysis with * indicating $p < 0.05$.

MBGN (SiO_2-CaO system) would show no antibacterial effects due to the absence of antibacterial metal species. Moreover, their dissolution products could not significantly raise local pH to an extent inducing bacteria death [18]. Ag is well-known for its broad-spectrum bactericidal activity, which is usually not compromised after its combination with BG [22]. Ag in various forms has shown the antibacterial activity, though antibacterial mechanisms and effects are diverse for different Ag species [15,45]. We then evaluated the ion release ability of Ag-MBGN. The concentration of released Ag^+ ions from Ag-MBGN was measured to be 672 ± 113 μg/L (~6×10^{-6} M) after 24 h soaking in PBS at the concentration of 1 mg/mL, which confirmed the ion release behavior of Ag-MBGN and indicated the possible reason of their antibacterial action (release of Ag^+ ions). As discussed above, in addition to the incorporated Ag^+ ions, Ag-MBGN also contained metallic Ag NPs (Fig. 4a). Due to the co-existence of Ag^+ and metallic Ag NPs, Ag-MBGN are expected to have a long-term antibacterial activity. The doped Ag^+ ions can be released in a relatively short time to kill bacteria [22,50]. At variance with doped ions, metallic Ag NPs only slowly release Ag^+ ions through oxidation, which is usually inhibited under physiological conditions [15]. Therefore, Ag NPs are expected to maintain their metallic state and property of inhibiting bacterial activity by binding to the membrane of bacteria [15] and/or by continuously generating ROS [46] for a relatively long-term. The stability of Ag NPs in Ag-MBGN was also proven by the XRD results where the diffraction peaks of Ag NPs could still be observed in Ag-MBGN after 7 days in SBF (Fig. 5b).

Previous studies in the literature [10,22,24,53] have reported the presence of a possible concentration window of Ag-related biomaterials that is safe for mammalian cells but toxic towards bacterial cells. For example, Ning et al. [53] have reported that the concentration level (10^{-7} M to 10^{-6} M) of Ag^+ ions was safe to fibroblast cells but toxic towards bacteria. However, it should be pointed out that the experimental conditions (*e.g.*, cell density, salt concentrations, protein contents) which could affect the cytotoxic effects of Ag were usually different between the antibacterial tests and human cell tests. For example, Ag^+ ions can interact with proteins and amino acids in the culture medium to form complexes, leading to reduced antibacterial effects [54]. On the other hand, Greulich et al. [45] reported that the effective cytotoxic concentration of Ag towards bacteria and human cells (*i.e.*, human mesenchymal stem cells and peripheral blood mononuclear cells) was nearly identical under a comparable culture condition in the planktonic bacteria model. Therefore, the determination and location of the therapeutic concentration window of Ag-containing biomaterials need further investigations that must consider the influence of environmental factors (*e.g.*, salt concentrations, protein

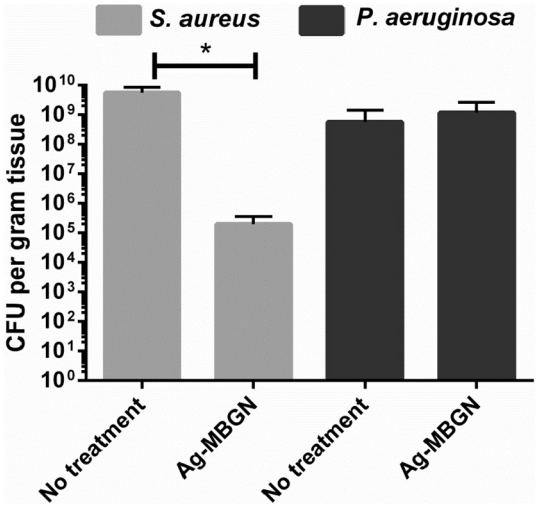

Fig. 8. Antibacterial properties of Ag-MBGN tested using the 3D tissue engineered infected skin model with established biofilms/infections of either *S. aureus* or *P. aeruginosa*. A significant reduction in *S. aureus* bacteria is observed from the models whereas no impact of Ag-MBGN was observed against *P. aeruginosa*. Three technical repeats (n = 3) were used within each experiment that was repeated in triplicate (N = 3). Data presented as mean ± standard deviation (SD), and ANOVA was used for statistical analysis with * indicating $p < 0.05$.

contents). Particularly, the influence of proteins that widely exist *in vivo* should be considered as their presence may reduce the antibacterial activity of Ag [45]. Ag-MBGN could adsorb proteins readily in physiological fluids, due to their large specific surface area and porous structure. The adsorbed proteins could then affect the properties of Ag-MBGN (*e.g.*, dissolution, mineralization) [55], which would influence their ion release behavior and antibacterial effect [45]. Furthermore, the antibacterial effect of Ag^+ ions could also be inhibited due to their interactions with proteins or other biomolecules in tissues or culture media to form complexes [56,57]. In a planktonic bacteria model, these factors are usually not fully considered, and the obtained results may not represent the actual antibacterial activity of Ag-MBGN *in vivo*. As an attempt to more realistically measure the antibacterial effects of Ag-MBGN, we then assessed their antibacterial activity in a 3D tissue-engineered infected skin model, in which the intricate interactions occurring *in vivo*, for example, bacteria invasion and interaction with different cell types in a complex three-dimensional solid structure, can be mimicked to some extent [29].

Fig. 8 shows the number of viable bacteria remaining in the infected tissue after treatment with Ag-MBGN. A significant reduction of *S. aureus* bacteria was observed from the models whereas no impact of Ag-MBGN against *P. aeruginosa* was observed. This result was different from our observations with planktonic bacteria (Fig. 7), in which Ag-MBGN could reduce the number of both bacteria. The reduced antibacterial effect of Ag-MBGN against *P. aeruginosa* might be due to the invasive nature of *P. aeruginosa* in the infected skin model. *P. aeruginosa* is far more invasive than *S. aureus* and penetrates much further into the skin layers than *S. aureus* does [29,35]. Ag-MBGN and released Ag^+ ions or generated ROS probably did not adequately penetrate through the skin layers to exert the antibacterial action against *P. aeruginosa* that are deeper down in the skin, at variance with *S. aureus* bacteria which were located much closer to the skin surface and thus could be more easily targeted by Ag-MBGN. The inhibited penetration of Ag^+ ions could be caused by their interactions with proteins and biomolecules in the 3D skin model. Abuayyash et al. [57] evaluated the antibacterial activity of Ag-containing thin films in a 3D tissue-like plasma clot matrix. Their results revealed that the consistency of a surrounding tissue could reduce the antibacterial activity of released Ag^+ ions due to the presence of higher total protein concentrations in comparison to the planktonic bacteria model. Similarly, the interactions between Ag and serum proteins *in vivo* could also significantly reduce the antibacterial activity of Ag while the minimized interactions with serum proteins could retain its antibacterial activity [58]. Therefore, enhanced antibacterial action in the 3D skin model or *in vivo* could be achieved by modulating the protein interactions with Ag-MBGN. The different antibacterial activities of Ag-MBGN shown in planktonic and 3D models reflect the complex situation associated to *in vivo* conditions, suggesting that in order to effectively treat bacteria-infected tissues, the development of devices, whose antibacterial species (*e.g.*, released ions, generated ROS) can reach the pathogens deeply in tissues and can penetrate established biofilms, must be addressed. In addition, the duration of the antibacterial effect of Ag-MBGN under the 3D tissue model condition should also be clarified in future studies.

4. Conclusions

Ag could be successfully incorporated into MBGN through a convenient surface modification approach. The morphology and mesoporous structure of nanoparticles were maintained after the modification, as evidenced by the similar particle sizes (100 to 250 nm) and pore sizes (2 to 9 nm) before and after the incorporation of Ag. The functionalization also did not reduce the bioactivity of the particles, as apatite formation could be observed on the particles after immersion in SBF for 3 days. Ag-MBGN could effectively inhibit clinically relevant bacteria (*S. aureus* and *P. aeruginosa*) at a concentration of 1 mg/mL while not inducing cytotoxicity against fibroblasts *in vitro*. The assessment in the 3D tissue-engineered infected skin model clearly showed the different antibacterial effects of Ag-MBGN against the two investigated bacteria strains, presenting a difference with the antibacterial behavior in the planktonic bacteria model. In the 3D skin model, Ag-MBGN could not effectively inhibit *P. aeruginosa* that invaded deeper into the dermis while inhibited *S. aureus* that was located much closer to the skin surface. Considering the morphological advantages (*e.g.*, nanoscale size, mesoporous structure), apatite-forming ability and antibacterial activity, Ag-MBGN show potential for applications related to infected tissue regeneration. However, a more effective antibacterial activity for Ag-MBGN to treat infected 3D tissues is still required. The possibility to exploit Ag antibacterial effects by using Ag-MBGN as drug delivery carriers remains a subject for interesting future research.

Acknowledgment

This project has received funding from the European Union's Horizon 2020 research and innovation programme under grant agreement No. 685872-MOZART (www.mozartproject.eu). Mr. Xinlong Hu (East China University of Science and Technology, Shanghai) is acknowledged for the nitrogen sorption measurement. Mr. Christian Scholz (Institute of Environmental Geochemistry, University of Heidelberg, Germany) is thanked for the ICP-OES measurement. We thank Prof. Wolfgang Peukert and Prof. Dirk Schubert (University of Erlangen-Nuremberg) for access to experimental facilities in their Institutes.

References

[1] J.R. Jones, Reprint of: review of bioactive glass: from Hench to hybrids, Acta Biomater. 23 (2015) S53–S82, https://doi.org/10.1016/j.actbio.2015.07.019.
[2] V. Miguez-Pacheco, L.L. Hench, A.R. Boccaccini, Bioactive glasses beyond bone and teeth: emerging applications in contact with soft tissues, Acta Biomater. 13 (2015) 1–15, https://doi.org/10.1016/j.actbio.2014.11.004.
[3] K. Zheng, A.R. Boccaccini, Sol-gel processing of bioactive glass nanoparticles: a review, Adv. Colloid Interf. Sci. 249 (2017) 363–373, https://doi.org/10.1016/j.cis.2017.03.008.
[4] C. Vichery, J.-M. Nedelec, Bioactive glass nanoparticles: from synthesis to materials design for biomedical applications, Materials (Basel) 9 (2016) 288–295, https://doi.

org/10.3390/ma9040288.
[5] Y. Yang, K. Zheng, R. Liang, A. Mainka, N. Taccardi, J.A. Roether, R. Detsch, W.H. Goldmann, S. Virtanen, A.R. Boccaccini, Cu-releasing bioactive glass/poly-caprolactone coating on Mg with antibacterial and anticorrosive properties for bone tissue engineering, Biomed. Mater. 13 (2018) 015001, , https://doi.org/10.1088/1748-605X/aa87f2.
[6] K. Zheng, J. Wu, W. Li, D. Dippold, Y. Wan, A.R. Boccaccini, Incorporation of Cu-containing bioactive glass nanoparticles in gelatin coated scaffolds enhances bioactivity and osteogenic activity, ACS Biomater Sci. Eng. 4 (2018) 1546–1557, https://doi.org/10.1021/acsbiomaterials.8b00051.
[7] C.D.F. Moreira, S.M. Carvalho, H.S. Mansur, M.M. Pereira, Thermogelling chitosan–collagen–bioactive glass nanoparticle hybrids as potential injectable systems for tissue engineering, Mater. Sci. Eng. C 58 (2016) 1207–1216, https://doi.org/10.1016/j.msec.2015.09.075.
[8] S. Kaya, M. Cresswell, A.R. Boccaccini, Mesoporous silica-based bioactive glasses for antibiotic-free antibacterial applications, Mater. Sci. Eng. C 83 (2017) 99–107.
[9] A. Hoppe, N.S. Güldal, A.R. Boccaccini, A review of the biological response to ionic dissolution products from bioactive glasses and glass-ceramics, Biomaterials 32 (2011) 2757–2774, https://doi.org/10.1016/j.biomaterials.2011.01.004.
[10] J.H. Lee, A. El-Fiqi, N. Mandakhbayar, H.H. Lee, H.W. Kim, Drug/ion co-delivery multi-functional nanocarrier to regenerate infected tissue defect, Biomaterials 142 (2017) 62–76, https://doi.org/10.1016/j.biomaterials.2017.07.014.
[11] W. Fan, Y. Wu, T. Ma, Y. Li, B. Fan, Substantivity of Ag–Ca–Si mesoporous nanoparticles on dentin and its ability to inhibit Enterococcus faecalis, J. Mater. Sci. Mater. Med. 27 (2016) 16–25, https://doi.org/10.1007/s10856-015-5633-x.
[12] C.R. Arciola, D. Campoccia, L. Montanaro, Implant infections: adhesion, biofilm formation and immune evasion, Nat. Rev. Microbiol. 16 (2018) 397–409, https://doi.org/10.1038/s41579-018-0019-y.
[13] A. Simchi, E. Tamjid, F. Pishbin, A.R. Boccaccini, Recent progress in inorganic and composite coatings with bactericidal capability for orthopaedic applications, Nanomedicine 7 (2011) 22–39, https://doi.org/10.1016/j.nano.2010.10.005.
[14] J. Davies, D. Davies, Origins and evolution of antibiotic resistance, Microbiol. Mol. Biol. Rev. 74 (2010) 417–433, https://doi.org/10.1128/MMBR.00016-10.
[15] K. Gold, B. Slay, M. Knackstedt, A.K. Gaharwar, Antimicrobial activity of metal and metal-oxide based nanoparticles, Adv. Ther. 1 (2018) 1700033, , https://doi.org/10.1002/adtp.201700033.
[16] D. Campoccia, L. Montanaro, C.R. Arciola, A review of the clinical implications of anti-infective biomaterials and infection-resistant surfaces, Biomaterials 34 (2013) 8018–8029, https://doi.org/10.1016/j.biomaterials.2013.07.048.
[17] J.A. Lemire, J.J. Harrison, R.J. Turner, Antimicrobial activity of metals: mechanisms, molecular targets and applications, Nat. Rev. Microbiol. 11 (2013) 371–384, https://doi.org/10.1038/nrmicro3028.
[18] I. Allan, H. Newman, M. Wilson, Antibacterial activity of particulate Bioglass® against supra- and subgingival bacteria, Biomaterials 22 (2001) 1683–1687, https://doi.org/10.1016/S0142-9612(00)00330-6.
[19] D. Zhang, O. Leppäranta, E. Munukka, H. Ylänen, M.K. Viljanen, E. Eerola, et al., Antibacterial effects and dissolution behavior of six bioactive glasses, J. Biomed. Mater. Res. A 93 (2010) 475–483, https://doi.org/10.1002/jbm.a.32564.
[20] F.E. Ciraldo, E. Boccardi, V. Melli, F. Westhauser, A.R. Boccaccini, Tackling bioactive glass excessive in vitro bioreactivity: preconditioning approaches for cell culture tests, Acta Biomater. 75 (2018) 3–10, https://doi.org/10.1016/j.actbio.2018.05.019.
[21] S. Chernousova, M. Epple, Silver as antibacterial agent: ion, nanoparticle, and metal, Angew. Chem. Int. Ed. 52 (2013) 1636–1653, https://doi.org/10.1002/anie.201205923.
[22] M. Bellantone, H.D. Williams, L.L. Hench, B.B. Activity, Broad-spectrum bactericidal activity of Ag_2O-doped bioactive, Antimicrob. Agents Chemother. 46 (2002) 1940–1945, https://doi.org/10.1128/AAC.46.6.1940.
[23] H.N. Wilkinson, S. Iveson, P. Catherall, M.J. Hardman, A novel silver bioactive glass elicits antimicrobial efficacy against Pseudomonas aeruginosa and Staphylococcus aureus in an ex vivo skin wound biofilm model, Front. Microbiol. 9 (2018) 1450–1466, https://doi.org/10.3389/fmicb.2018.01450.
[24] A.M. El-Kady, A.F. Ali, R.A. Rizk, M.M. Ahmed, Synthesis, characterization and microbiological response of silver doped bioactive glass nanoparticles, Ceram. Int. 38 (2012) 177–188, https://doi.org/10.1016/j.ceramint.2011.05.158.
[25] D. Kozon, K. Zheng, E. Boccardi, Y. Liu, L. Liverani, A.R. Boccaccini, Synthesis of monodispersed Ag-doped bioactive glass nanoparticles via surface modification, Materials (Basel) 9 (2016) 225–233, https://doi.org/10.3390/ma9040225.
[26] C. Wang, Y. Xie, A. Li, H. Shen, D. Wu, D. Qiu, Bioactive nanoparticle through postmodification of colloidal silica, ACS Appl. Mater. Interfaces 6 (2014) 4935–4939.
[27] S.J. Shih, W.L. Tzeng, R. Jatnika, C.J. Shih, K.B. Borisenko, Control of Ag nanoparticle distribution influencing bioactive and antibacterial properties of Ag-doped mesoporous bioactive glass particles prepared by spray pyrolysis, J Biomed Mater Res B Appl Biomater 103 (2015) 899–907, https://doi.org/10.1002/jbm.b.33273.
[28] R. Phetnin, S.T. Rattanachan, Preparation and antibacterial property on silver incorporated mesoporous bioactive glass microspheres, J. Sol-Gel Sci. Technol. 75 (2015) 279–290, https://doi.org/10.1007/s10971-015-3697-1.
[29] J. Shepherd, I. Douglas, S. Rimmer, L. Swanson, S. Macneil, Development of three-dimensional tissue-engineered models of bacterial infected human skin wounds, Tissue Eng. Part C Methods 15 (2009) 475–484, https://doi.org/10.1089/ten.tec.2008.0614.
[30] Q. Liang, Q. Hu, G. Miao, B. Yuan, X. Chen, A facile synthesis of novel mesoporous bioactive glass nanoparticles with various morphologies and tunable mesostructure by sacrificial liquid template method, Mater. Lett. 148 (2015) 45–49, https://doi.org/10.1016/j.matlet.2015.01.122.
[31] T. Meincke, V.M. Pacheco, D. Hoffmann, A.R. Boccaccini, R.N.K. Taylor, Engineering the surface functionality of 45S5 bioactive glass-based scaffolds by the heterogeneous nucleation and growth of silver particles, J. Mater. Sci. 52 (2017) 9082–9090, https://doi.org/10.1007/s10853-017-0877-0.
[32] H. Bao, W. Peukert, R.N.K. Taylor, One-pot colloidal synthesis of plasmonic patchy particles, Adv. Mater. 23 (2011) 2644–2649, https://doi.org/10.1002/adma.201100698.
[33] T. Kokubo, H. Takadama, How useful is SBF in predicting in vivo bone bioactivity? Biomaterials 27 (2006) 2907–2915, https://doi.org/10.1016/j.biomaterials.2006.01.017.
[34] A.J. Hedges, R. Shannon, R.P. Hobbs, Comparison of the precision obtained in counting viable bacteria by the spiral plate maker, the droplette and the Miles & Misra methods, J. Appl. Bacteriol. 45 (1978) 57–65.
[35] J. Shepherd, P. Sarker, S. Rimmer, L. Swanson, S. MacNeil, I. Douglas, Hyperbranched poly(NIPAM) polymers modified with antibiotics for the reduction of bacterial burden in infected human tissue engineered skin, Biomaterials 32 (2011) 258–267, https://doi.org/10.1016/j.biomaterials.2010.08.084.
[36] S. Brunauer, L.S. Deming, W.E. Deming, E. Teller, On a theory of the van der Waals adsorption of gases, J. Am. Chem. Soc. 62 (1940) 1723–1732.
[37] N. Pal, E.-B. Cho, A.K. Patra, D. Kim, Ceria-containing ordered mesoporous silica: synthesis, properties, and applications, ChemCatChem 8 (2016) 285–303, https://doi.org/10.1002/cctc.201500780.
[38] J.C. Kung, Y.J. Chen, Y.C. Chiang, C.L. Lee, Y.T. Yang-Wang, C.C. Hung, et al., Antibacterial activity of silver nanoparticle (AgNP) confined mesoporous structured bioactive powder against Enterococcus faecalis infecting root canal systems, J. Non-Cryst. Solids 502 (2018) 62–70, https://doi.org/10.1016/j.jnoncrysol.2018.06.030.
[39] H. Aguiar, J. Serra, P. González, B. León, Structural study of sol-gel silicate glasses by IR and Raman spectroscopies, J. Non-Cryst. Solids 355 (2009) 475–480, https://doi.org/10.1016/j.jnoncrysol.2009.01.010.
[40] M. Cerruti, C. Morterra, Carbonate formation on bioactive glasses, Langmuir 20 (2004) 6382–6388, https://doi.org/10.1021/la049723c.
[41] K. Zheng, M. Lu, B. Rutkowski, X. Dai, Y. Yang, N. Taccardi, et al., ZnO quantum dots modified bioactive glass nanoparticles with pH-sensitive release of Zn ions, fluorescence, antibacterial and osteogenic properties, J. Mater. Chem. B 4 (2016) 7936–7949, https://doi.org/10.1039/C6TB02053D.
[42] F.Y. Fan, M.S. Chen, C.W. Wang, S.J. Shih, C.Y. Chen, Y.N. Pan, et al., Preparation and characterization of silver nanocrystals decorated mesoporous bioactive glass via synchrotron X-ray reduction, J. Non-Cryst. Solids 450 (2016) 128–134, https://doi.org/10.1016/j.jnoncrysol.2016.08.012.
[43] Y.F. Goh, A.Z. Alshemary, M. Akram, M.R. Abdul Kadir, R. Hussain, Bioactive glass: an in-vitro comparative study of doping with nanoscale copper and silver particles, Int. J. Appl. Glas. Sci. 266 (2014) 255–266, https://doi.org/10.1111/ijag.12061.
[44] A. Vulpoi, C. Gruian, E. Vanea, L. Baia, S. Simon, H.J. Steinhoff, et al., Bioactivity and protein attachment onto bioactive glasses containing silver nanoparticles, J. Biomed. Mater. Res. A 100 A (2012) 1179–1186, https://doi.org/10.1002/jbm.a.34060.
[45] C. Greulich, D. Braun, A. Peetsch, J. Diendorf, B. Siebers, M. Epple, et al., The toxic effect of silver ions and silver nanoparticles towards bacteria and human cells occurs in the same concentration range, RSC Adv. 2 (2012) 6981–6987, https://doi.org/10.1039/c2ra20684f.
[46] M. Lv, S. Su, Y. He, Q. Huang, W. Hu, D. Li, et al., Long-term antimicrobial effect of silicon nanowires decorated with silver nanoparticles, Adv. Mater. 22 (2010) 5463–5467, https://doi.org/10.1002/adma.201001934.
[47] L.L. Hench, Opening paper 2015- some comments on bioglass: four eras of discovery and development, Biomed. Glasses 1 (2015) 1–11, https://doi.org/10.1515/bglass-2015-0001.
[48] K. Zheng, A. Solodovnyk, W. Li, O.-M. Goudouri, C. Stähli, S.N. Nazhat, et al., Aging time and temperature effects on the structure and bioactivity of gel-derived 45S5 glass-ceramics, J. Am. Ceram. Soc. 98 (2015) 30–38, https://doi.org/10.1111/jace.13258.
[49] J. Serra, P. González, S. Liste, C. Serra, S. Chiussi, B. León, et al., FTIR and XPS studies of bioactive silica based glasses, J. Non-Cryst. Solids 332 (2003) 20–27, https://doi.org/10.1016/j.jnoncrysol.2003.09.013.
[50] M. Bellantone, N.J. Coleman, L.L. Hench, Bacteriostatic action of a novel four-component bioactive glass, J. Biomed. Mater. Res. 51 (2000) 484–490.
[51] E. Vernè, S. Di Nunzio, M. Bosetti, P. Appendino, C. Vitale Brovarone, G. Maina, et al., Surface characterization of silver-doped bioactive glass, Biomaterials 26 (2005) 5111–5119, https://doi.org/10.1016/j.biomaterials.2005.01.038.
[52] H. Wang, S. Zhao, X. Cui, Y. Pan, W. Huang, S. Ye, et al., Evaluation of three-dimensional silver-doped borate bioactive glass scaffolds for bone repair: biodegradability, biocompatibility, and antibacterial activity, J. Mater. Res. 30 (2015) 2722–2735, https://doi.org/10.1557/jmr.2015.243.
[53] C. Ning, X. Wang, L. Li, Y. Zhu, M. Li, P. Yu, et al., Concentration ranges of antibacterial cations for showing the highest antibacterial efficacy but the least cytotoxicity against mammalian cells: implications for a new antibacterial mechanism, Chem. Res. Toxicol. 28 (2015) 1815–1822, https://doi.org/10.1021/acs.chemrestox.5b00258.
[54] S. Kittler, C. Greulich, J. Diendorf, M. Köller, M. Epple, Toxicity of silver nanoparticles increases during storage because of slow dissolution under release of silver ions, Chem. Mater. 22 (2010) 4548–4554, https://doi.org/10.1021/cm100023p.
[55] K. Zheng, M. Kapp, A.R. Boccaccini, Protein interactions with bioactive glass surfaces: a review, Appl. Mater. Today 15 (2019) 350–371, https://doi.org/10.1016/j.apmt.2019.02.003.
[56] J.B. Wright, K. Lam, R.E. Burrell, Wound management in an era of increasing bacterial antibiotic resistance: a role for topical silver treatment, Am. J. Infect. Control 26 (1998) 572–577, https://doi.org/10.1053/ic.1998.v26.a93527.
[57] A. Abuayyash, N. Ziegler, J. Gessmann, C. Sengstock, T.A. Schildhauer, A. Ludwig, et al., Antibacterial efficacy of sacrifical anode thin films combining silver with platinum group elements within a bacteria-containing human plasma clot, Adv. Eng. Mater. 20 (2018) 1700493, , https://doi.org/10.1002/adem.201700493.
[58] D.P. Gnanadhas, M. Ben Thomas, R. Thomas, A.M. Raichur, D. Chakravortty, Interaction of silver nanoparticles with serum proteins affects their antimicrobial activity in vivo, Antimicrob. Agents Chemother. 57 (2013) 4945–4955, https://doi.org/10.1128/AAC.00152-13.